

Preparation of LDO@TiO₂ core-shell nanosheets for enhanced photocatalytic degradation of organic pollutions

Can Wang^a, Ruikang Zhang^{a,*}, Yucong Miao^b, Qihui Xue^a, Borong Yu^a, Yuanzhe Gao^a, Zhan-gang Han^a, Mingfei Shao^b

^a*Hebei Key Laboratory of Organic Functional Molecules, College of Chemistry and Materials Science, Hebei Normal University, Shijiazhuang, Hebei 050024, China.*

^b*State Key Laboratory of Chemical Resource Engineering, Beijing University of Chemical Technology, Beijing 100029, China*

E-mail: zhangruikang@hebtu.edu.cn

Abstract: TiO₂-based nanosheets materials with core-shell structure are expected to be one of the promising photocatalysts to degradation of organic pollutions. However, it is a challenge to synthesis of TiO₂ shell on functional core materials by desired nucleation and growth process. Layered double hydroxides (LDHs) are considered as ideal platforms to *in-situ* grow TiO₂ and further serve as additional components to construct heterojunction to improve the separation of photo-generated charge carriers. In this work, we report the design and fabrication of anatase TiO₂ coated ZnAl-layered double oxide (LDO@TiO₂) nanosheets, which involves the *in-situ* growth of TiO₂ on ZnAl-LDH followed by a subsequent calcination treatment. The resulting LDO@TiO₂ photocatalyst gives typical core-shell nanosheets morphology with mesoporous structure, which exhibiting excellent photodegradation and mineralization efficiency for organic pollutions.

Keywords: LDO@TiO₂ nanosheets; core-shell; LDHs; photocatalysts; photodegradation

1 Introduction

Photodegradation is a promising technology to remove the organic pollutants from wastewater, which can directly utilize solar energy to mineralize pollutants (e.g., dyes, antibiotics and aromatic

compounds) into CO₂ and H₂O [1–5]. Photocatalysts play a key role in the photodegradation process, and many semiconductors (e.g., TiO₂ [6], α-Fe₂O₃ [7], WO₃ [8] and BiVO₄ [9]) have been studied as photocatalyst for photodegradation. Because of the excellent stability and catalytic activity, TiO₂ is expected to be one of the promising photocatalysts. In recent years, nanosheets [10], nanorods [11], nanotubes [12] and microspheres [13] TiO₂ materials with control of crystallinity and exposed facets have been reported. The nanostructured TiO₂ materials present efficient active sites and large surface area, resulting in enhanced photocatalytic degradation performance [14–16]. However, the inherent low electron mobility and short hole diffusion length of TiO₂ bring about intense charge recombination, and hinders their photocatalytic activity.

The photodegradation process involves the generation, separation of charge carriers and the following redox reactions of pollutants [17–21]. To enhance the photocatalytic degradation performance of TiO₂, it is an efficient method to fabricate TiO₂-based composite photocatalysts. For example, building TiO₂/NiO heterojunction can enhance the separation of photogenerated electron-hole pairs [22]; introducing graphene oxide to TiO₂ facilitates the generation of O₂^{•-} and HO[•] radicals, thereby improving the photocatalytic activities towards organic pollutions [23]. Among the composite photocatalysts, core-shell structured materials attract lots of attention as they usually possess highly distinctive physical and chemical properties in the integrated system. For instance, TiO₂@Bi₂W_xMo_{1-x}O₆ core-shell nanofibers possess boosting visible light absorption and reduced charge recombination rate, exhibiting good photocatalytic activities towards tetracycline hydrochloride [24]; CoTiO₃ coated nanosheets-assembled TiO₂ nanospheres can promote the photodegradation of antibiotics due to the enhanced charge separation efficiency and mass transfer [25]; However, the reported TiO₂-based core-shell photocatalysts mostly are TiO₂ as shell material, which is disadvantage of the exposure of catalytic activity sites in TiO₂. In addition, nanosheet photocatalysts are recognized as an ideal structure to reduce the charge migration distance and further suppress the charge recombination [26–28]. Therefore, it is attractive to fabricate TiO₂-based

core-shell nanosheets materials, especially TiO₂ as shell-materials with enhanced photocatalytic performance. However, it is a challenge to synthesis of TiO₂ shell on functional core materials by desired nucleation and growth process.

Layered double hydroxides (LDHs) are typical two-dimensional cationic clays with the general formula $[M^{II}_{1-x}M^{III}_x(OH)_2]^{x+} (A^{n-}_{x/n})^m H_2O$, where M^{II} and M^{III} are bivalent and trivalent metal cations, Aⁿ⁻ are interlayer anions (CO₃²⁻, Cl⁻, SO₄²⁻ etc.). The structure of M^{II}M^{III}-LDHs is orderly formed by positive charged metal layer $[M^{II}_{1-x}M^{III}_x(OH)_2]$ and interlayer anions for charge compensation [29–31]. The unsaturated coordination state of LDHs surface is advantage of the nucleation and growth of extrinsic components [32–34]. The hydroxyl group in metal layer can provide reaction sites for the hydrolysis of titanium precursor. After calcination of LDHs, the obtained layer double oxides (LDOs) are composite of mixed metal oxides and can be considered as a new type of semiconductor materials. For example, ZnAl-LDO and NiTi-LDO has been reported as excellent photocatalysts [35, 36]. Therefore, LDHs nanosheets are promising platforms to *in-situ* grow TiO₂ and further serve as additional components to construct heterojunction or other functional materials to improve the separation of photo-generated charge carriers.

Herein, we report the design and fabrication of anatase TiO₂ coated ZnAl-LDO (LDO@TiO₂) nanosheets, which involves the *in-situ* growth of TiO₂ on ZnAl-LDH followed by a subsequent calcination treatment. The resulting LDO@TiO₂ photocatalyst gives typical core-shell nanosheets morphology with mesoporous structure. The ZnAl-LDO core material is consisting of zincite ZnO and amorphous Al₂O₃, and TiO₂ shell material is anatase TiO₂. The ZnAl-LDO/TiO₂ heterojunction in the core/shell interface facilitate the charge separation and further promote the photodegradation of dyes. Consequently, LDO@TiO₂ photocatalysts exhibits excellent photodegradation and mineralization efficiency for organic dyes. This work provides an elaborate strategy for the preparation of TiO₂ nanosheets heterojunction materials using LDHs as platform, which has potential applications in the field of photocatalysts.

2 Experiments

2.1 Materials

ZnCl₂, Al(NO₃)₃ · 9H₂O, tetrabutyl titanate [Ti(OBu)₄], urea, ethanol, 5,5-dimethyl-1-pyrroline N-oxidewere (DMPO), Na₂SO₄, rutile TiO₂ were purchased from Shanghai Aladdin Bio-Chem Technology Co., LTD. P25 TiO₂ was purchased from Aeroxide Degussa, Germany. The water used in all experiments was purified through a Millipore system.

2.2 Preparation of ZnAl-LDH and ZnAl-LDO

ZnAl-LDH was prepared in a three-neck flask equipped with a reflux condenser under a nitrogen flow [37]. Typically, ZnCl₂ (4 mmol), Al(NO₃)₃ · 9H₂O (2 mmol) and urea (14 mmol) were dissolved in 400 mL of deionized water. The solution was then heated at 97 °C under refluxing and continuous stirring for 24 h. The resulting product was washed with ethanol for several times, and finally dried in air.

The as-prepared ZnAl-LDH was placed in a ceramic boat and transferred into a muffle furnace. ZnAl-LDO-*T* (*T* = 200, 400, 600, 800 °C) were obtained with calcination temperature at 200, 400, 600, 800 °C, respectively, in the air for 2 h with a heating rate of 5 °C min⁻¹. ZnAl-LDO-600 was abbreviated as ZnAl-LDO.

2.3 Preparation of LDH@TiO₂ and LDO@TiO₂

LDH@TiO₂ was synthesized by solvothermal method. Typically, 1.2 g ZnAl-LDH was dispersed into 25 mL 99.5 % ethanol solution, and then 0.4 mL Ti(OBu)₄ was added into the above solution under magnetic stirring at room temperature. Then, the solutions were aged in a 50 mL teflon-lined stainless steel autoclave at 100 °C for 12 h. After cooling down to room temperature, the LDH@TiO₂ samples were washed several times with deionized water, and finally dried in air. For preparation of LDH@TiO₂-L and LDH@TiO₂-H, 0.2 mL and 0.6 mL Ti(OBu)₄ were added into the ethanol solution, respectively. The other processes were performed by the same method of LDH@TiO₂.

LDO@TiO₂-*T* was obtained by roasting LDH@TiO₂ with the same calcination process as ZnAl-LDO. LDO@TiO₂-600 was abbreviated as LDO@TiO₂.

2.4 Characterization

The morphology was investigated using a scanning electron microscopy (SEM; Hitachi, S-4800). X-ray diffraction (XRD) patterns were collected on a Rigaku XRD-6000 diffractometer using Cu K α radiation with a scan step of 10 ° min⁻¹. Thermogravimetric (TG) curves were collected on a STA449F3/TENSOR27 TG/DTA instrument under N₂ atmosphere with a heating rate of 10 °C min⁻¹. X-ray photoelectron spectra (XPS) were recorded on a Thermo VG Escalab 250 with Al K α X-rays as the excitation source. Transmission electron microscopy (TEM) images were collected on recorded using a Philips Tecnai 20 and JEOL JEM-2010 high-resolution transmission electron microscopes. X-ray spectrometry (EDS) elemental mapping were operated with a probe focused to 0.2 nm. The specific surface area, pore volume and size analysis were performed by Brunauer-Emmett-Teller and Barrett-Joyner-Halenda method, respectively, using a Kubo-X1000 analyzer. Solid UV–Vis diffuse reflection spectra and UV–Vis adsorption spectra was characterized using an Agilent Cary 60 spectrophotometer. Electron paramagnetic resonance (EPR) dates were collected on a Bruker E500 EPR spectrometer at room temperature with a 300 W Xe lamp as illuminant. Total organic carbon (TOC) was determined using TOC-L (Shimadzu, Japan).

2.5 Photocatalytic degradation experiments

Methylene blue (MB, cationic dye) and acid orange (AO, anion dye) were used as representative organic pollutions to investigated the photocatalytic activity of prepared samples. The illumination source was a 150 W Xe lamp under AM 1.5G simulated solar irradiation with a power density of 100 mW cm⁻². The degradation experiment was carried out on a home-made 250 mL glass reactor. Photocatalyst (50 mg) was firstly dispersed to 100 mL aqueous solution MB (10 mg L⁻¹) or AO (25 mg L⁻¹). The suspension was magnetically stirred in the dark for 40 min to ensure adsorption-desorption equilibrium. Then, irradiation was carried out, and this point was recorded as

the initiation time. At certain time intervals, 4 mL of the suspension was removed and filtered using a 0.22 μm filter for analysis. The concentration of MB (or AO) was analyzed by measuring the absorbance at maximum wavelength of 664 nm (484 nm) using a UV-vis spectrophotometer. The degradation or TOC removal ratios were calculated according to the equation: $(C_0 - C_t)/C_0 \times 100 \%$ or $(\text{TOC}_0 - \text{TOC}_t)/\text{TOC}_0 \times 100 \%$, where C_0 and TOC_0 are the initial concentrations of dyes; C_t and TOC_t are the concentrations of dyes at reaction time.

2.6 Photoelectrochemical measurements

A homogeneous suspension was prepared by dispersing 10 mg as-prepared photocatalyst in 2 mL ethanol. Then, 50 μL of the suspension was dip-coated on the fluorine-doped tin oxide ($2\text{ cm} \times 2\text{ cm}$) followed by drying in a vacuum oven at 60 $^{\circ}\text{C}$ for 2h. Photocurrent measurements were conducted on an electrochemical workstation (CHI 660e, CH Instruments Inc., Shanghai) in 0.1 M Na_2SO_4 aqueous solution with a conventional three-electrode cell. The illumination source was a 150 W Xe lamp under AM 1.5G simulated solar irradiation with a power density of 100 mW cm^{-2} . The as-obtained ZnAl-LDO and LDO@TiO₂ as working electrode were immersed in the electrolyte. The Pt wire as counter electrode, saturated calomel electrode (SCE) as the reference electrode are installed in a quartz cell.

3 Results and discussion

3.1 Materials preparation and characterization

The preparation process of TiO₂ coated ZnAl-LDO (LDO@TiO₂) core-shell nanosheets is illustrated in Figure 1a, which involves the *in-situ* growth of TiO₂ on ZnAl-LDH nanosheets followed by a subsequent calcination process. ZnAl-LDH nanosheets were firstly prepared by a reported hydrothermal process, and it presents typical hexagonal platelets with thickness of 100–200 nm and diameter of 2–5 μm (Figure 1b). Then, amorphous TiO₂ was *in-situ* growing on the surface of ZnAl-LDH nanosheets by the controllable hydrolysis of tetrabutyl titanate $[\text{Ti}(\text{OBU})_4]$. The thickness of TiO₂ coated on ZnAl-LDH nanosheets (LDH@TiO₂) increase to 150–250 nm after the growth of

TiO₂ shell (Figure 1c). Finally, LDO@TiO₂ core-shell nanosheets were obtained after the calcination process at 600 °C, which inherits the morphology of LDH@TiO₂ (Figure 1d). In addition, ZnAl-LDO sample was prepared to give a comparison study by calcining ZnAl-LDH with the same conditions, which also shows lamellar morphology (Figure S1).

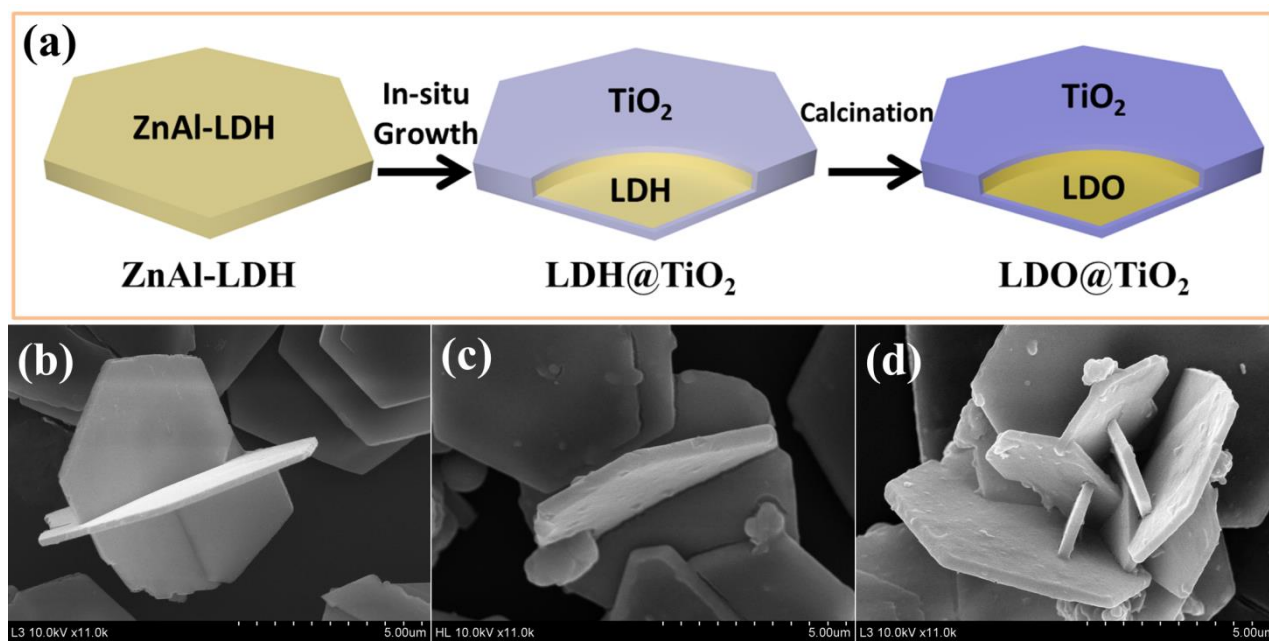


Figure 1. (a) Schematic illustration for the preparation process of LDO@TiO₂. SEM images of (b) ZnAl-LDH, (c) LDH@TiO₂ and (d) LDO@TiO₂, respectively.

The phase structure of ZnAl-LDH, LDH@TiO₂ and their derived calcined samples ZnAl-LDO, LDO@TiO₂ were investigated by X-ray diffraction (XRD) method. As shown in Figure 2a, ZnAl-LDH displays the typical (003), (006), (009) reflections at 12.2 °, 24.3 °, 36.0 °, respectively. No added reflection is observed in LDH@TiO₂, indicating the amorphous phase of TiO₂ shell. ZnAl-LDO shows a series of new reflections at 31.8 °, 34.4 ° and 36.3 ° corresponding to (100), (002) and (101) planes of zincite ZnO (PDF#36-1451). The absence of Al₂O₃ reflections demonstrates that ZnAl-LDO is consisting of zincite ZnO and amorphous Al₂O₃, which is consistent with previous report [38]. It is worth mention that the amorphous Al₂O₃ can enhance the structure stability of LDOs nanosheets. For LDO@TiO₂, the (101) plane of anatase TiO₂ at 25.3 ° (PDF#21-1272) and the reflections of ZnAl-LDO both can be observed in the XRD pattern. The superimposition of ZnO and

TiO_2 phases in LDO@TiO_2 demonstrate the effective combination of ZnAl-LDO and anatase TiO_2 . Furthermore, the effect of calcination temperature on the structural evolution phase conversion of ZnAl-LDH and LDH@TiO_2 was investigated. Thermogravimetric (TG) curves show that ZnAl-LDH presents three weight loss stages (Figure 2b). The first step (20–220 °C) has a ~13.5 % weight loss corresponds to the removal of crystal water and interlayer water. The second weight loss is ~13.6 % (220–350 °C), which can be ascribed to the dehydroxylation of the hydroxide layers and decomposition of the interlayer anions. The third step (weight loss ~4.2 % at 350–850 °C) is attributed to the decomposition of the rest dehydroxylation of the hydroxide layers [39]. LDH@TiO_2 also displays three weight loss stages as ZnAl-LDH. Because phase conversion process of TiO_2 has less weight loss during the heating process [40], the three steps weight loss of LDH@TiO_2 is only ~12.3 % (20–220 °C), ~8.5 % (220–350 °C) and ~2.6 % (350–850 °C), respectively. The XRD patterns of LDO@TiO_2 sample at four calcination temperatures (denoted as $\text{LDO@TiO}_2\text{-}T$; T is the temperature) confirms the results of TG. As shown in Figure 2c, $\text{LDO@TiO}_2\text{-}200$ displays weak reflections of LDH, indicating the reserve of lamellar structure of LDH. The (003) reflection of LDH at 12.2° disappears accompanied by the appearance of (002) facet of zincite ZnO at 34.4° in $\text{LDO@TiO}_2\text{-}400$, indicating the dehydroxylation of the hydroxide layers. The reflections of ZnO and anatase TiO_2 are both observed in $\text{LDO@TiO}_2\text{-}600$ (denoted as LDO@TiO_2). The (112), (103), (224) planes of Zn_2TiO_4 (PDF#19-1483) at 29.9°, 35.2°, 62.1° and (220) (311) planes of ZnAl_2O_4 (PDF#05-0669) at 31.2°, 36.8° are observed in $\text{LDO@TiO}_2\text{-}800$, suggesting that TiO_2 , ZnO and Al_2O_3 convert to the cubic spinel phase (Zn_2TiO_4 and ZnAl_2O_4). ZnAl-LDO- T samples show similar phases compared with the corresponding $\text{LDO@TiO}_2\text{-}T$ sample but without the phases containing Ti element (Figure S2). For example, only (220) (311) planes of ZnAl_2O_4 are observed in ZnAl-LDO-800. These results indicate that ZnAl-LDO can maintain structure stability in a wide calcination temperature.

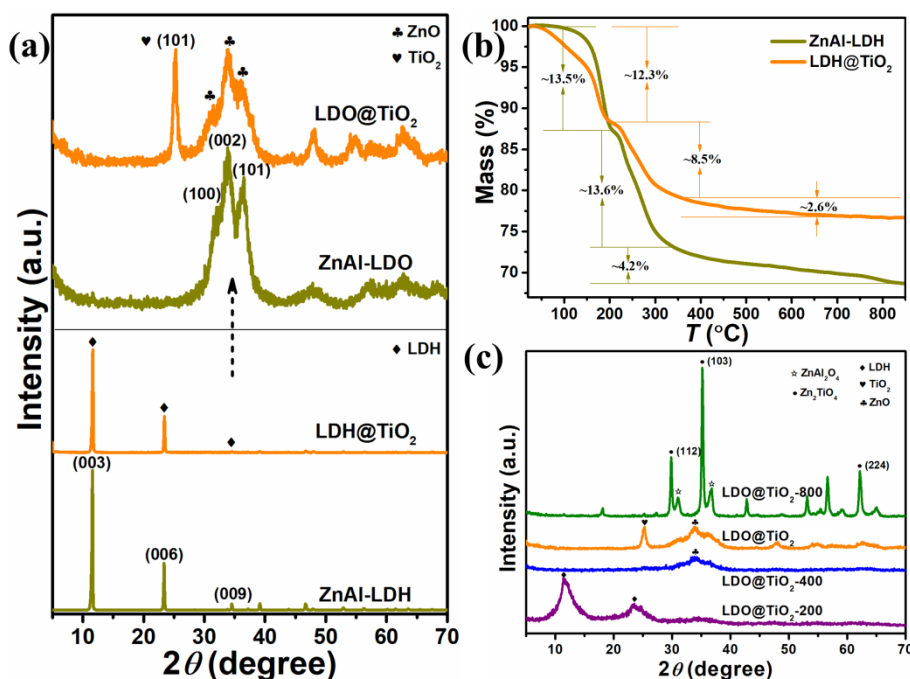


Figure 2. (a) XRD patterns of ZnAl-LDH, LDH@TiO₂, ZnAl-LDO and LDO@TiO₂. (b) TG curves of ZnAl-LDH and LDH@TiO₂. (c) XRD patterns of LDO@TiO₂-*T* samples.

The transmission electron microscopy (TEM) image of a sliced LDH@TiO₂ nanosheet confirms the core-shell structure. TiO₂ shell layer was uniformly coated on the LDH core nanosheet, and the thickness of ZnAl-LDH core and TiO₂ shell is ~300 and ~80 nm, respectively (Figure 3a). No lattice fringe appears in the shell material, confirming that TiO₂ is amorphous (Figure S3). LDO@TiO₂ displays similar core-shell structure of LDH@TiO₂ (Figure 3b). Porous structure can be observed in core and shell region, deriving from the release of gaseous species (H₂O, CO₂ etc.) during the calcination process of ZnAl-LDH [41]. The corresponding energy dispersive X-ray spectrometry (EDS) mapping verify the well-defined ZnAl oxides core and Ti oxide shell structure: the Zn and Al elements show a high density in the core region while Ti element is located in the shell region (Figure 3c). The high-resolution transmission electron microscopy (HRTEM) image of LDO@TiO₂ reveals that ZnAl-LDH core and amorphous TiO₂ shell of LDH@TiO₂ have convert to ZnAl-LDO and anatase TiO₂ phases (Figure 3d). In shell region, the interplanar distance of 0.352 nm corresponds to the (101) plane of anatase TiO₂ [42]. The interplanar distances of 0.248 nm, 0.260 nm and 0.281 nm in core region can be ascribed to the (100), (002), and (101) planes of zincite ZnO,

respectively [43]. The surface area and pore size distribution of prepared samples were investigated by N₂-adsorption/desorption measurements. The type-IV isotherm with H3-type hysteresis loops ($P/P_0 > 0.4$) is both observed for LDO and LDO@TiO₂ (Figure 3e). The specific surface area of ZnAl-LDH is relatively low (7.9 m² g⁻¹). ZnAl-LDO has an enhanced specific surface area (43.8 m² g⁻¹), and LDO@TiO₂ further increases to 73.8 m² g⁻¹. ZnAl-LDO presents mesoporous distribution with the main pore size of 8–9 nm (Figure 3f). For LDO@TiO₂, the pore sizes distribute with two peaks (4–5 and 8–9 nm). It can be inferred from the TEM images that the 4–5 and 8–9 nm mesoporous of LDO@TiO₂ mainly corresponds to the porous TiO₂ shell and ZnAl-LDO core, respectively. The mesoporous distribution of LDO@TiO₂ is advantage of adsorption and desorption of dyes.

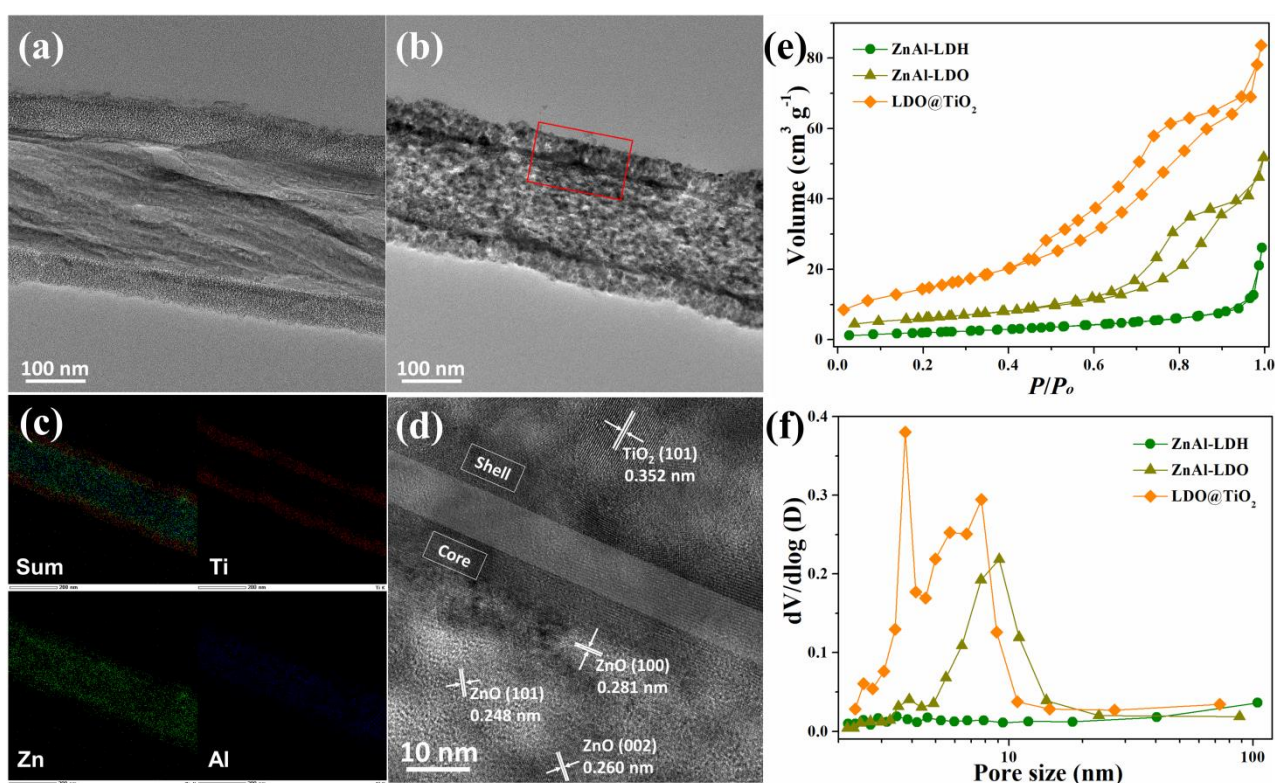


Figure 3. TEM images of (a) LDH@TiO₂ and (b) LDO@TiO₂. (c) EDS mapping and (d) HRTEM image of LDH@TiO₂. (e) N₂-sorption isotherms and (f) pore-size distribution of ZnAl-LDH, ZnAl-LDO and LDO@TiO₂, respectively.

Furthermore, it is found that the growth of TiO₂ shell on ZnAl-LDH can be controlled by the concentration of Ti(OBu)₄ in the hydrothermal solution (see details in the experimental section). The

SEM images of two samples obtained in low and high concentrations of $\text{Ti}(\text{OBu})_4$ (denoted as $\text{LDH@TiO}_2\text{-L}$, $\text{LDH@TiO}_2\text{-H}$) are shown in Figure 4a and 4b, respectively. The thickness of $\text{LDH@TiO}_2\text{-L}$ nanosheet is much thinner than that of LDH@TiO_2 , suggesting that small amount of TiO_2 was coated in the ZnAl-LDH. $\text{LDH@TiO}_2\text{-H}$ nanosheet displays thick TiO_2 shell, and some TiO_2 microspheres can be observed outside the core-shell materials (Figure S4). These experimental results demonstrate that LDH@TiO_2 fabricated in a middle concentration of $\text{Ti}(\text{OBu})_4$ can be considered as an optimal sample in this work. Based on the hydrolysis mechanism of $\text{Ti}(\text{OBu})_4$, the *in-situ* growth process of TiO_2 on ZnAl-LDH was schematically shown in Figure 4c. The $-\text{OH}$ group and absorbed water molecules in LDH surface provide polar reaction environment, so the dealcoholization of $\text{Ti}(\text{OBu})_4$ preferentially reacts on the surface of ZnAl-LDH. The intermediate $\text{Ti}(\text{OH})_4$ keeps the going of hydrolysis process [44]. The hydrolysis process gradually reaches equilibrium as the consumption of $\text{Ti}(\text{OBu})_4$. Finally, amorphous TiO_2 was *in-situ* grown on the surface of LDHs nanosheets to form core-shell structure.

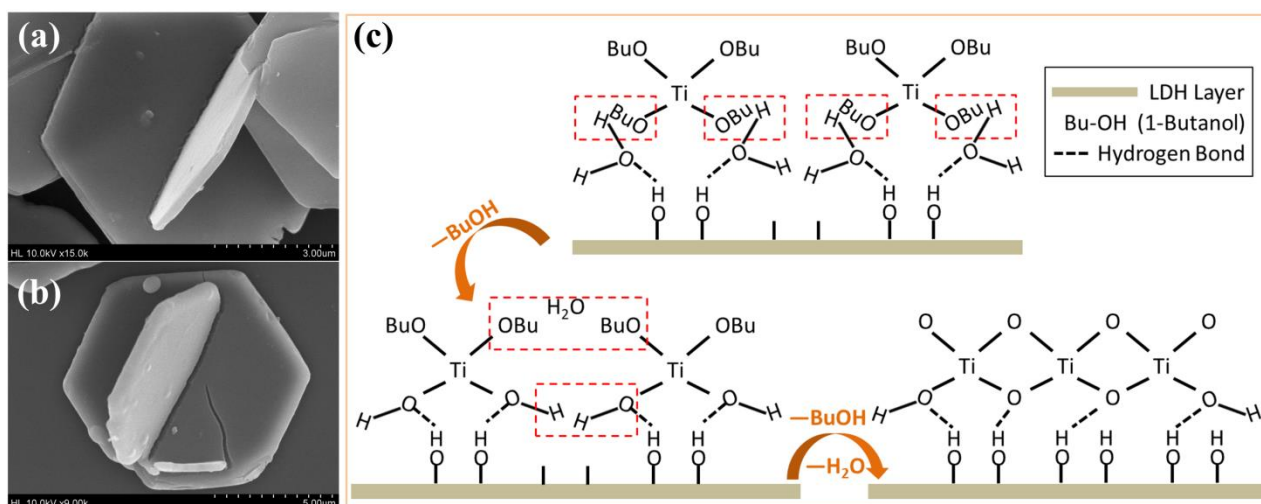


Figure 4. SEM images of (a) $\text{LDH@TiO}_2\text{-L}$ and (b) $\text{LDH@TiO}_2\text{-H}$. (c) the proposed pathways for the *in-situ* growth process of TiO_2 on the ZnAl-LDH surface.

3.2 Photocatalytic degradation performance

The photocatalytic degradation performance of organic pollutions was evaluated by degradation of methylene blue (MB, a typical cationic dye) and acid orange (AO, a typical anion dye) in neutral

aqueous solution (Commercial P25 was used as a control photocatalyst). The concentration of MB or AO was analyzed by measuring the absorbance at maximum wavelength of 664 nm or 484 nm using a UV–vis spectrophotometer, respectively (Figure S5 and S6). The absorption properties of MB and AO for LDO@TiO₂, ZnAl-LDO and P25 TiO₂ photocatalysts were distinctly different (Figure 6a). The adsorption efficiency of MB and AO for P25 were both relatively low. LDO@TiO₂ and ZnAl-LDO display 10.9 % and 9.1 % adsorption efficiency of MB, which is similar with P25. But for the anionic AO, the adsorption efficiency of LDO@TiO₂ and ZnAl-LDO dramatically increased to 51.2 % and 70.8 %, respectively. The high adsorption efficiencies can be attributed to the regeneration of ZnAl-LDH which bringing with the chemical adsorption of anionic AO. It was reported that LDOs can convert to LDHs due to the “memory effect” when it contacts with water solutions containing with anions [45]. The (003), (006) reflections at 12.2 °, 24.3 ° appears in the XRD patterns of used LDO@TiO₂ and ZnAl-LDO, demonstrating the regeneration of ZnAl-LDH (Figure S7). The reservation of the reflections of ZnO indicates that only a part of ZnAl-LDO convert to ZnAl-LDH. To eliminate the effect of dyes adsorption, the used photocatalysts were mixed with dye solutions for 40 min to reach the adsorption-desorption equilibrium before the irradiation reaction.

Under irradiation reaction, the MB photodegradation efficiency of ZnAl-LDO is 41.7 % within 120 min, which is lower than that of P25 (Figure 5b). This result indicates that pristine ZnAl-LDO is a bad photocatalyst. LDO@TiO₂ displays much enhanced degradation efficiency (86.4 %), deriving from the synergy of ZnAl-LDO core and TiO₂ shell. For the anionic AO, the degradation efficiencies of three samples also give the following order: LDO@TiO₂ > P25 > ZnAl-LDO. The AO degradation efficiencies of three samples are higher than that of MB, indicating that the adsorption of dyes on surface of photocatalysts facilitates to the degradation process. Furthermore, the total organic carbon (TOC) analysis was measured to determine the mineralization efficiencies of dyes by the photocatalytic degradation reaction (Figure 5c). The TOC removal efficiency of ZnAl-LDO is

inferior to P25, which is only 24.8 % (MB) and 28.8 % (AO) in 120 min. The TOC removal efficiency of LDO@TiO₂ increases to 63.7 % (MB) and 70.9 % (AO), suggesting that MB and AO can be mostly mineralized to H₂O and CO₂ by the photocatalytic process of LDO@TiO₂. In addition, the stability of the LDO@TiO₂ was carried out by a cycle photocatalytic degradation reaction of MB and AO. It exhibits nearly constant photodegradation performance after three cycles, indicating the good stability of the photocatalyst (Figure 5d). The above results demonstrate that LDO@TiO₂ core-shell material is an excellent photocatalysis for photodegradation of organic pollutions.

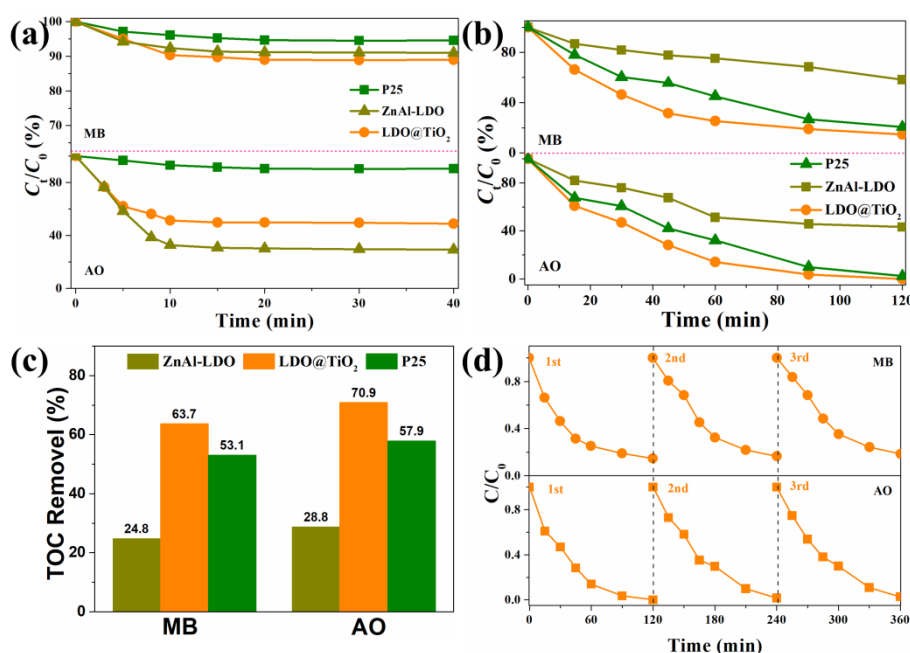


Figure 5. (a) Absorption efficiency, (b) photodegradation efficiency and (c) TOC removal efficiency of MB and AO for ZnAl-LDO, LDO@TiO₂ and P25, respectively. (d) cycle experiments of LDO@TiO₂ for MB and AO photocatalytic degradation reaction.

3.3 Mechanism discussion

Further investigated were carried out to give a deep insight into the enhanced photocatalytic degradation performance of LDO@TiO₂. The elemental valence state of LDO@TiO₂, ZnAl-LDO and commercial anatase TiO₂ (TiO₂-Anatase) were studied by X-ray photoelectron spectroscopy (XPS). The full spectrum of LDO@TiO₂ reveals signals of Zn, Al, Ti and O element (Figure S8). As shown in Figure 6a, O 1s XPS spectrum can be deconvoluted into two peaks at 530.0 eV and 531.7

eV, which is assigned to the lattice oxygen O^{2-} and surface $-OH$ group, respectively. The surface $-OH$ group is considered as one of the main defects in metal oxides [46]. Strong $-OH$ peak is observed in ZnAl-LDO, which is consistent with the reports that LDO materials are hydrophilic on account of the "memory effect" [47]. TiO_2 -Anatase displays a typical strong O^{2-} peak. LDO@ TiO_2 present the weakest $-OH$ group peak and the strongest O^{2-} peak, suggesting that the surface defect of LDO and TiO_2 are suppressive due to the synergy of core and shell components. Two dominant peaks at 1022.6 and 1045.7 eV corresponding to Zn $2p_{3/2}$ and $2p_{1/2}$ are observed in ZnAl-LDO (Figure 6b). The binding energies of Zn^{2+} status is close to Zn-OH than Zn-O, which is consistent with the O 1s XPS spectrum. After the incorporation of TiO_2 shell, two peaks of Zn 2p decrease to 1021.7 and 1044.8 eV, indicating the increase of Zn-O and decrease of Zn-OH bond in LDO@ TiO_2 . TiO_2 -Anatase shows the binding energies of 458.6 and 464.3 eV for Ti $2p_{3/2}$ and Ti $2p_{1/2}$, respectively. A negative shift (0.5 eV) of Ti 2p peaks is observed in LDO@ TiO_2 , indicating a distinct increase in the electron density of Ti (Figure 6c). This remarkable negative shift suggests the electron transfer from ZnAl-LDO to TiO_2 group in LDO@ TiO_2 .

In addition, the bandgap of ZnAl-LDO and LDO@ TiO_2 were estimated by the UV-vis absorption spectra (Figure 6d). ZnAl-LDO exhibit light absorption edge at 420 nm, corresponding to the band gap of 3.0 eV. The absorption edge of LDO@ TiO_2 and TiO_2 -Anatase are both located at ~390 nm, confirming the successful formation of anatase TiO_2 in the core-shell photocatalyst. The electron paramagnetic resonance (EPR) measurements of LDO@ TiO_2 and ZnAl-LDO were shown in Figure 6e. Under light irradiation, DMPO- OH (peak intensity ratio = 1 : 2 : 2 : 1) signals are observed in ZnAl-LDO and LDO@ TiO_2 . The OH signal intensities of LDO@ TiO_2 are obviously higher than that of ZnAl-LDO under same irradiation time. Since the OH are derived from isolated photogenerated holes, the improved signal intensities of LDO@ TiO_2 indicates a higher separation efficiency for the photo-generated electron-hole pairs [48]. Photoelectrochemical experiments under on-off cyclical light were further performed to probe the interface charge transfer behaviors (Figure

6f). ZnAl-LDO displays a relatively low photocurrent response. The photocurrent density of LDO@TiO₂ has a remarkable improvement, suggesting the lower recombination of photo-generated carriers.

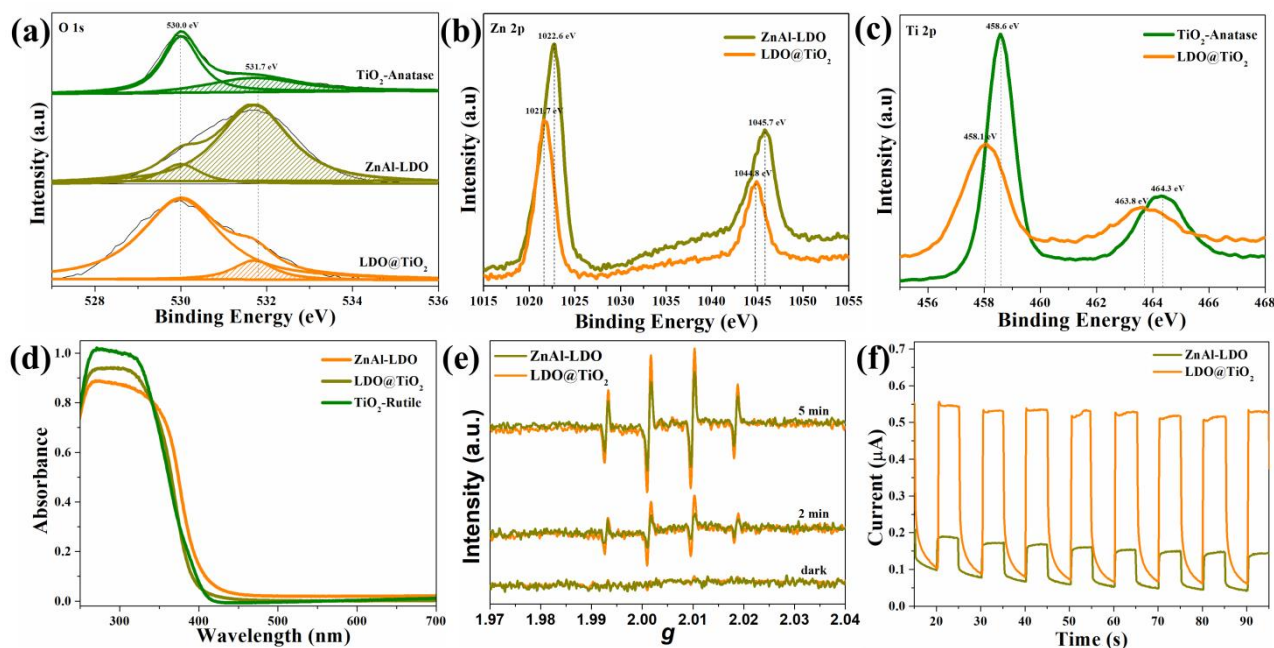


Figure 6. (a) O 1s XPS of TiO₂, ZnAl-LDO and LDO@TiO₂, respectively. (b) Zn 2p XPS of ZnAl-LDO and LDO@TiO₂. (c) Ti 2p XPS of TiO₂ and LDO@TiO₂. (d) UV-vis diffuse reflectance spectra of ZnAl-LDO, LDO@TiO₂ and TiO₂-Rutile, respectively. (e) EPR spectra and (f) photocurrents of ZnAl-LDO and LDO@TiO₂, respectively.

Given the results above, a mechanism for the enhanced photocatalytic degradation performance of LDO@TiO₂ is proposed (Figure 7). The organic dyes molecules can diffuse across the mesoporous TiO₂ shell to interior ZnAl-LDO. The high specific surface of LDO@TiO₂ provides sufficient reactive sites. Under illumination, electron-hole pairs would generate both in ZnAl-LDO and TiO₂. Due to the band energy difference of ZnAl-LDO and TiO₂ [49, 50], the photogenerated holes on the valence band of TiO₂ tend to migrate to ZnAl-LDO while the photogenerated electrons of ZnAl-LDO travel to TiO₂. The opposite migration in the ZnAl-LDO/TiO₂ heterojunction interface hinders the recombination of charge carriers, which has been confirmed by the EPR and photoelectrochemical experiment results. The generation of OH on the surface of TiO₂ and ZnAl-LDO can efficiently decompose organic dyes molecules to low molecules (CO₂ etc.). The

mesoporous structure of nanosheets facilitates the diffusion of reactants and products. Therefore, LDO@TiO₂ core-shell nanosheets exhibit excellent photocatalytic degradation performances.

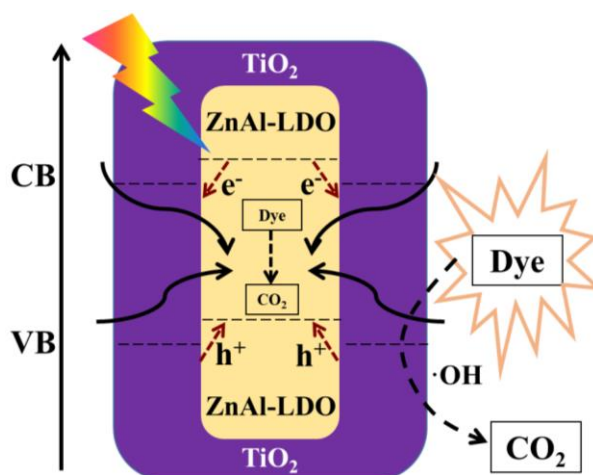


Figure 7. A schematic illustration for the photodegradation process of LDO@TiO₂ core-shell nanosheets.

4 Conclusions

In conclusion, LDO@TiO₂ core-shell nanosheets photocatalyst were designed and successfully prepared by the transformation of LDH@TiO₂ precursor. The fabrication process of TiO₂ shell and LDOs core can be facilely controlled by the concentration of Ti(OBu)₄ and LDHs processors. The prepared LDO@TiO₂ photocatalyst gives typical core-shell nanosheets morphology with mesoporous structure and high specific surface area. TEM, XPS and photoelectrochemical analyses demonstrate the successful fabrication of ZnAl-LDO/TiO₂ core-shell heterojunction, which facilitate the charge separation efficiency. Consequently, LDO@TiO₂ photocatalysts exhibits superior photodegradation and mineralization ratio for organic pollutions. It is expected that this LDO@TiO₂ fabrication strategy can be applicable to preparation of other core-shell metal oxide composite materials.

Acknowledgements

This work was supported by the Natural Science Foundation of Hebei Province (B2020205006, B2021205027), the National Natural Science Foundation of China (21902042, 21871076), and the Science Foundation of Hebei Normal University (L2019B14).

Reference

- [1] Sofian, K.; Matthew, A. M.; Robert, B. A.; Howard, H. P. Recent advances on TiO₂-based photocatalysts toward the degradation of pesticides and major organic pollutants from water bodies. *Catal. Rev.* **2019**, *62*, 1–65.
- [2] Huang, X. P.; Chen, Y.; Eric, W.; Zong, M. R.; Wang, Y.; Zhang, X.; Odeta, Q.; Wang, Z. M.; Kevin, M. R. Facet-Specific Photocatalytic Degradation of Organics by Heterogeneous Fenton Chemistry on Hematite Nanoparticles. *Environ. Sci. Technol.* **2019**, *53*, 10197–10207.
- [3] Hassan, A.; Asad, M.; Jechan, L.; Ki-H, K.; Jae-W, P.; Alex, C. K. Y. Photocatalysts for degradation of dyes in industrial effluents: Opportunities and challenges. *Nano Res.* **2020**, *12*, 9462–9470.
- [4] Wang, Y. T.; Zhu, C. Z.; Zuo, G. C.; Guo, Y.; Xiao, W.; Dai, Y. X.; Kong, J. J.; Xu, X. M.; Zhou, Y. X.; Xie, A.; Sun, C.; Xian, Q. M. 0D/2D Co₃O₄/TiO₂ Z-Scheme heterojunction for boosted photocatalytic degradation and mechanism investigation. *Appl. Catal. B* **2020**, *278*, 119298.
- [5] Wan, D.; Wang, J.; Dionysios, D. D.; Kong, Y. Q.; Yao, W. Y.; Steplinska, S.; Chen, Y. Photogeneration of Reactive Species from Biochar-Derived Dissolved Black Carbon for the Degradation of Amine and Phenolic Pollutants. *Environ. Sci. Technol.* **2021**, *55*, 8866–8876.
- [6] Monteagudo, J. M.; Durán, A.; Martín, I. S.; Carrillo, P. Effect of sodium persulfate as electron acceptor on antipyrine degradation by solar TiO₂ or TiO₂/rGO photocatalysis. *Chem. Eng. J.* **2019**, *364*, 257–268.
- [7] Zhang, R. B.; Du, B.; Li, Q. C.; Cao, Z. Q.; Feng, G.; Wang, X. W. α -Fe₂O₃ nanoclusters confined into UiO-66 for efficient visible-light photodegradation performance. *Appl. Surf. Sci.* **2019**, *466*, 956–963.

- [8] Zhu, W. Y.; Liu, J. C.; Yu, S. Y.; Zhou, Y.; Yan, X. L. Ag loaded WO₃ nanoplates for efficient photocatalytic degradation of sulfanilamide and their bactericidal effect under visible light irradiation. *J. Hazard. Mater.* **2016**, *318*, 407–416.
- [9] Liu, H. B.; Hou, H. L.; Gao, F. M.; Yao, X. H.; Yang, W.Y. Tailored Fabrication of BiVO₄ Thoroughly Mesoporous Nanofibers and Their Visible-Light Photocatalytic Activities. *ACS Appl. Mater. Interfaces* **2016**, *8*, 1929–1936.
- [10] Meng, A.Y.; Zhang, J.; Xu, D. F.; Cheng, B.; Yu, J.G. Enhanced photocatalytic H₂ -production activity of anatase TiO₂ nanosheet by selectively depositing dual-cocatalysts on {101} and {001} facets. *Appl. Catal. B* **2016**, *198*, 286–294.
- [11] Huang, X. Q.; Zhang, R. K.; Gao, X. R.; Yu, B. R.; Gao, Y. Z.; Han, Z. Z. TiO₂-rutile/anatase homojunction with enhanced charge separation for photoelectrochemical water splitting. *Int. J. Hydrog. Energy* **2021**, *46*, 26358–26366.
- [12] Wang, Q.; Huang, J.;Y.; Sun, H.; T.; Zhang, K.; Q.; Lai, Y.; K. Uniform carbon dots@TiO₂ nanotube arrays with full spectrum wavelength light activation for efficient dye degradation and overall water splitting. *Nanoscale* **2017**, *9*, 16046–16058.
- [13] Wei, H.; McMaster, W. A.; Jeannie, Z. Y. T.; Chen, D. H.; Rachel, A. C. Tricomponent brookite/anatase TiO₂/g-C₃N₄ heterojunction in mesoporous hollow microspheres for enhanced visible-light photocatalysis. *J. Mater. Chem. A* **2018**, *6*, 7236–7245.
- [14] Sadaf, B. K.; Hou, M. J. ; Shuang, S.; Zhang, Z. J. Morphological influence of TiO₂ nanostructures (nanozigzag, nanohelics and nanorod) on photocatalytic degradation of organic dyes. *Appl. Surf. Sci.* **2017**, *400*, 184–193.
- [15] Amarja, P. N.; Hemant, M.; Vijay, S. W.; Laxmi, S.; Abhijeet, R.; Saeed, M. A.; Ali, A. A.;

- Sheshanath, V. B. Pranay P Morajkar. Super porous TiO₂ photocatalyst: Tailoring the agglomerate porosity into robust structural mesoporosity with enhanced surface area for efficient remediation of azo dye polluted waste water. *J. Environ. Manage.* **2020**, 258, 110029.
- [16]Kisung, L.; Hyewon, Yoon.; Changui, A.; Jun,Y. P.; Seokwoo, J. Strategies to improve the photocatalytic activity of TiO₂: 3D nanostructuring and heterostructuring with graphitic carbon nanomaterials. *Nanoscale* **2019**, 11, 7025–7040.
- [17]Chen, D. Y.; Zhu, H. G.; Yang, S.; Li, N.J.; Xu, Q. F.; Li, H.; He, J. H.; Lu, J. M. Micro-Nanocomposites in Environmental Management. *Adv. Mater.* **2016**, 28, 10443–10458.
- [18]Chen, Z.; Li, X. M.; Xu, Q. Z.; Tao, Z. L.T.; Yao, F. B.; Huang, X. D.; Wu, Y.; Wang, D. B.; Jiang, P. H.; Yang, Q. Three-dimensional network space Ag₃PO₄/NP-CQDs/rGH for enhanced organic pollutant photodegradation: Synergetic photocatalysis activity/stability and effect of real water quality parameters. *Chem. Eng. J.* **2020**, 390, 124454.
- [19]Zong, M. R.; Song, D.; Zhang, X.; Huang, X. P.; Lu, X. C.; Kevin M. R. Facet-Dependent Photodegradation of Methylene Blue by Hematite Nanoplates in Visible Light. *Environ. Sci. Technol.* **2021**, 55, 677–688.
- [20]Guo, Y.; Wang, P. F.; Qian, J.; Ao, Y. H.; Wang, C.; Hou, J. Phosphate group grafted twinned BiPO₄ with significantly enhanced photocatalytic activity: Synergistic effect of improved charge separation efficiency and redox ability. *Appl. Catal. B* **2018**, 234, 90–99.
- [21]Chen, P.; Lee, B.; Giovanni, C.; Huang, J.; Wang, B.; Wang,Y. J.; Deng, S. B.; Gang, Y. Degradation of Ofloxacin by Perylene Diimide Supramolecular Nanofiber Sunlight-Driven Photocatalysis. *Environ. Sci. Technol.* **2019**, 53, 1564–1575.
- [22]Chen, J.; Wang, M. G.; Han, J.; Guo, R. TiO₂ nanosheet/NiO nanorod hierarchical nanostructures:

- p-n heterojunctions towards efficient photocatalysis. *J. Colloid Interface Sci.* **2020**, *562*, 313–321.
- [23] Samuel, O. -B. O.; Francis, O.; Penny, P. G. Tuning the electronic and structural properties of Gd-TiO₂-GO nanocomposites for enhancing photodegradation of IC dye: The role of Gd³⁺ ion. *Appl. Catal. B* **2019**, *243*, 106–120.
- [24] Seyed, M. G.; Kugalur, S. R.; Hoomin, L.; Hong, I. J.; Somayeh, Z. N.; Young, K. H.; Yun, S. H. Hierarchical N-doped TiO₂@Bi₂W_xMo_{1-x}O₆ core-shell nanofibers for boosting visible-light-driven photocatalytic and photoelectrochemical activities. *J. Hazard. Mater.* **2020**, *391*, 122249.
- [25] Li, H.T.; Gao, Q. ; Wang, G. S.; Han, B.; Xia, K. S.; Zhou, C. G. Architecturing CoTiO₃ overlayer on nanosheets-assembled hierarchical TiO₂ nanospheres as a highly active and robust catalyst for peroxymonosulfate activation and metronidazole degradation. *Chem. Eng. J.* **2020**, *392*, 123819.
- [26] Zhong, H.; Yang, C.; Fan, L. Z.; Fu, Z. H.; Yang, X.; Wang, X. C.; Wang, R. H. Dyadic promotion of photocatalytic aerobic oxidation via the Mott–Schottky effect enabled by nitrogen-doped carbon from imidazolium-based ionic polymers. *Energy Environ. Sci.* **2019**, *12*, 418–426.
- [27] Wang, L.; Zhang, Y.; Chen, L.; Xu, H. X.; Xiong, Y. J. 2D Polymers as Emerging Materials for Photocatalytic Overall Water Splitting. *Adv. Mater.* **2018**, *30*, 1801955.
- [28] Lian, X. Y.; Xue, W. H.; Dong, S.; Liu, E. Z.; Li, H.; Xu, K. Z. Construction of S-scheme Bi₂WO₆/g-C₃N₄ heterostructure nanosheets with enhanced visible-light photocatalytic degradation for ammonium dinitramide. *J. Hazard. Mater.* **2021**, *412*, 125217.
- [29] Willinton, Y. H.; Jeroen, L.; Pascal, V. D. V.; An, V. Recent advances on the utilization of layered double hydroxides (LDHs) and related heterogeneous catalysts in a lignocellulosic-feedstock biorefinery scheme. *Green Chem.* **2017**, *19*, 5269–5302.

- [30] Lu, Z. Y.; Qian, L.; Xu, W. W.; Tian, Y.; Jiang, M.; Li, Y. P.; Sun, X. M.; Duan, X. Dehydrated layered double hydroxides: Alcohothermal synthesis and oxygen evolution activity. *Nano Res.* **2016**, *9*, 3152–3161.
- [31] Chen, X.; Wang, H. N.; Xia, B.; Meng, R. R. Noncovalent phosphorylation of CoCr layered double hydroxide nanosheets with improved electrocatalytic activity for the oxygen evolution reaction. *Chem. Commun.* **2019**, *55*, 12076–12079.
- [32] Wu, C. C.; Li, H. Q.; Xia, Z. X.; Zhang, X. M.; Deng, R. Y.; Wang, S. L.; Sun, G. Q. NiFe Layered Double Hydroxides with Unsaturated Metal Sites via Pre-covered Surface Strategy for Oxygen Evolution Reaction. *ACS Catal.* **2020**, *10*, 11127–11135.
- [33] Lin, Y. P.; Wang, H.; Peng, C. K.; Bu, L. M.; Chiang, C. L.; Tian, K.; Zhao, Y.; Zhao, J. Q.; Lin, Y. G.; Jong, M. L.; Gao, L. J. Co-Induced Electronic Optimization of Hierarchical NiFe LDH for Oxygen Evolution. *Small* **2020**, *16*, 2002426.
- [34] Li, Y. F.; Zhang, R.K.; Li, J.M.; Liu, J. C.; Miao, Y. C.; Guo, J.; Shao, M. F. TiO₂/CuPc/NiFe-LDH photoanode for efficient photoelectrochemical water splitting. *Chin. Chem. Lett.* **2021**, *32*, 1165–1168.
- [35] Peng, D.; Jing, Q. Y.; Feng, Z. J.; Niu, J. W.; Cheng, X.; Wu, X.; Zheng, X. X.; Yuan, X. Y. Facile preparation of AB-stacking graphene oxide/ZnAl-layered double hydroxide composites and enhanced visible-light photocatalytic performance of the calcined product. *J. Phys. Chem. Solids* **2020**, *136*, 109199.
- [36] Zhao, Y. F.; Jia, X. D.; Chen, G. B.; Shang, L.; Geoffrey, I. N. W.; Wu, L. Z.; Tung, C. H.; Dermot O, H.; Zhang, T. R. Ultrafine NiO Nanosheets Stabilized by TiO₂ from Monolayer NiTi-LDH Precursors: An Active Water Oxidation Electrocatalyst. *J. Am. Chem. Soc.* **2016**, *138*, 6517–6524.

- [37]Cai, Y. J.; Song, H. Y.; An, Z.; Xiang, X.; Shu, X.; He, J. The confined space electron transfer in phosphotungstate intercalated ZnAl-LDHs enhances its photocatalytic performance for oxidation/extraction desulfurization of model oil in air. *Green Chem.* **2018**, *20*, 5509–5519.
- [38]Xu, Q.-H.; Xu, D.-M.; Guan, M.-Y.; Guo, Y. ; Qi, Q.; Li, G.-D. ZnO/Al₂O₃/CeO₂ composite with enhanced gas sensing performance. *Sens. Actuators B Chem.* **2013**, *177*, 1134–1141.
- [39]Meng, Q. T.; Yan, H. Theoretical study on the topotactic transformation and memory effect of M (II) M (III)-layered double hydroxides. *Mol. Simulat* **2017**, *43*, 1338–1347.
- [40]Rohini, S.; Suman, D. Synthesis and characterization of solar photoactive TiO₂ nanoparticles with enhanced structural and optical properties. *Adv Powder Technol* **2018**, *29*, 211–219.
- [41]Yuan, X. Y.; Jing, Q. Y.; Chen, J. T.; Li, L. Photocatalytic Cr(VI) reduction by mixed metal oxide derived from ZnAl layered double hydroxide. *Appl Clay Sci* **2017**, *143*, 168–174.
- [42]Jeong-A, P.; Boram, Y.; Joongki, L.; In, G. K.; Jae,-H. K.; Jae,-W. C.; Hee,-D. P.; In, W. N.; Sang,-H. L. Ultrasonic spray pyrolysis synthesis of reduced graphene oxide/anatase TiO₂ composite and its application in the photocatalytic degradation of methylene blue in water. *Chemosphere* **2018**, *191*, 738–746.
- [43]Liu, Y. j.; Huang, D.; Liu, H. X.; Li, T. D.; Wang, J. G. ZnO tetrakaidecahedrons with co-exposed {001}, {101}, and {100} facets: shape-selective synthesis and enhancing photocatalytic performance. *Cryst. Growth Des.* **2019**, *19*, 2758–2764.
- [44]Zhang, J.; Sun, P.; Jiang, P.; Guo, Z. Y.; Liu, W. X.; Lu, Q. P.; Cao, W. B. The formation mechanism of TiO₂ polymorphs under hydrothermal conditions based on the structural evolution of [Ti(OH)_h(H₂O)_{6-h}]^{4-h} monomers. *J. Mater. Chem. C* **2019**, *7*, 5764–5771.
- [45]Zong, Y. T.; Li, K.T.; Tian, R.; Lin,Y. J.; Lu, C. Highly dispersed layered double oxide hollow

spheres with sufficient active sites for adsorption of methyl blue. *Nanoscale* **2018**, *10*, 23191–23197.

[46] Miao, J.; Zhao, X. J.; Zhang, Y.-X.; Lei, Z.-L.; Liu, Z.-H. Preparation of hollow hierarchical porous CoMgAl-borate LDH ball-flower and its calcinated product with extraordinary adsorption capacity for Congo red and methyl orange. *Appl. Clay Sci.* **2021**, *207*, 106093.

[47] Li, M. Z.; Wu, G. H.; Liu, Z. H.; Xi, X. Y.; Xia, Y.; Ning, J.; Yang, D.; Dong, A. G. Uniformly coating ZnAl layered double oxide nanosheets with ultra-thin carbon by ligand and phase transformation for enhanced adsorption of anionic pollutants. *J. Hazard. Mater.* **2020**, *397*, 122766.

[48] Wu, Y.; Wang, H.; Sun, Y. M.; Xiao, T.; Tu, W. G.; Yuan, X. Z.; Zeng, G. M.; Li, S. J.; Chew, J. W. Photogenerated charge transfer via interfacial internal electric field for significantly improved photocatalysis in direct Z-scheme oxygen-doped carbon nitrogen/CoAl-layered double hydroxide heterojunction. *Appl. Catal. B* **2018**, *227*, 530–540.

[49] Wu, M. M.; Chang, B. W.; Teik, -T. Lim.; Wen, -D. O.; Lei, J. X.; Mi, J. High-sulfur capacity and regenerable Zn-based sorbents derived from layered double hydroxide for hot coal gas desulfurization. *J. Hazard. Mater.* **2018**, *360*, 391–401.

[50] Sun, C. Y.; Xu, Q. H.; Xie, Y.; Ling, Y.; Hou, Y. Designed synthesis of anatase–TiO₂ (B) biphasic nanowire/ZnO nanoparticle heterojunction for enhanced photocatalysis. *J. Mater. Chem. A* **2018**, *6*, 8289–8298.